Research Square

Preprints are preliminary reports that have not undergone peer review.
They should not be considered conclusive, used to inform clinical practice,
or referenced by the media as validated information.

Matrix stiffness-related transcriptomic signatures reveal astrocyte-centered neuroimmune alterations in Alzheimer's disease

Peida Luo
The First Affiliated Hospital of Henan University of Chinese Medicine
Yunhui Qiao
The First Affiliated Hospital of Henan University of Chinese Medicine
Chen Jin
The First Affiliated Hospital of Henan University of Chinese Medicine
Yinan Wang
The First Affiliated Hospital of Henan University of Chinese Medicine
Yanyan Qin
The First Affiliated Hospital of Henan University of Chinese Medicine
Yanru Wang
The First Affiliated Hospital of Henan University of Chinese Medicine
Yunke Zhang
henanzyk@126.com

The First Affiliated Hospital of Henan University of Chinese Medicine

Research Article

Keywords: Alzheimer's disease, matrix stiffness, extracellular matrix, astrocytes, neuroimmune remodeling, single-cell RNA sequencing, mechanotransduction

Posted Date: November 4th, 2026

DOI: https://doi.org/10.21203/rs.3.rs-11351463/v1

License: This work is licensed under a Creative Commons Attribution 4.0 International License.
Read Full License

Additional Declarations: No competing interests reported.

Matrix stiffness-related transcriptomic signatures reveal astrocyte-centered neuroimmune alterations in Alzheimer's disease

Peida Luo [1,2], Yunhui Qiao [1,2], Chen Jin [1,2], Yinan Wang [1,2], Yanyan Qin [1,2], Yanru Wang [1,2], Yunke Zhang [1, 3, *]

[1] Department of Encephalopathy, The First Affiliated Hospital of Henan University of Chinese Medicine, Zhengzhou, China

[2] The First Clinical Medical College of Henan University of Chinese Medicine, Zhengzhou, China

[3] Collaborative Innovation Center of Prevention and Treatment of Major Diseases by Chinese and Western Medicine, Henan Province, Zhengzhou 450000, China

Corresponding author(s):

Yunke Zhang, The First Clinical Medical College of Henan University of Chinese Medicine, Zhengzhou, China. Email: henanzyk@126.com.

Abstract

Background: Extracellular matrix remodeling and altered tissue mechanics are increasingly implicated in Alzheimer's disease (AD), but links between matrix stiffness and AD pathology remain unclear.

Objective: To identify matrix stiffness-related transcriptomic signatures in AD and characterize their diagnostic potential, functions, cell-type specificity, and intercellular communication patterns.

Methods: Bulk transcriptomic datasets from the Gene Expression Omnibus were integrated with literature-derived matrix stiffness-related genes. Differential expression analysis, three machine-learning algorithms, and cross-dataset validation were used to identify candidate genes and construct a multigene classification model. Functional enrichment and immune-cell deconvolution analyses were performed. Single-cell RNA sequencing data were analyzed to assess cell-type-specific expression, inferred astrocyte trajectories, and predicted cell–cell communication.

Results: Eighty-one differentially expressed matrix stiffness-related genes were identified in AD brain tissue. FREM3, DUSP4, and FAM107A were selected and showed concordant differential expression across discovery and validation datasets. The three-gene model achieved an area under the receiver operating characteristic curve of 0.963 in the discovery cohort. Gene set enrichment analysis linked all three genes to oxidative phosphorylation, although FAM107A showed an enrichment direction opposite to DUSP4 and FREM3. Immune deconvolution suggested associations with immune-cell signatures. Single-cell analysis identified astrocytes as a major population expressing the three-gene signature. AD astrocytes showed altered pseudotime distributions and stronger predicted communication with immune cells, particularly T cells and macrophages.

Conclusions: FREM3, DUSP4, and FAM107A are candidate matrix stiffness-related transcriptomic signatures in AD and may connect extracellular matrix remodeling with mitochondrial metabolism, immune dysregulation, and astrocyte-associated changes. Independent clinical validation and experimental confirmation are required.

Keywords: Alzheimer's disease, matrix stiffness, extracellular matrix, astrocytes, neuroimmune remodeling, single-cell RNA sequencing, mechanotransduction

Graphical Abstract



1. Introduction

Alzheimer's disease (AD) is a chronic neurodegenerative condition in which memory, cognition, executive function, and reasoning progressively deteriorate[1]. Because AD represents the leading cause of dementia in older adults, it poses a substantial global health burden and has been recognized as a public health priority[2, 3]. Pathologically, the disease is defined mainly by extracellular β-amyloid (Aβ) plaques and intracellular aggregates of hyperphosphorylated tau that form neurofibrillary tangles (NFTs)[4]. These lesions coexist with synaptic failure, neuronal loss, and gradual disruption of brain networks, ultimately causing irreversible cognitive impairment. The mechanisms driving AD remain unresolved despite extensive research. Although anti-amyloid therapies are now available for selected patients, their modest clinical benefit highlights the need for mechanism-informed biomarkers that can support early

stratification[5, 6]. Current therapeutic limitations also reflect the biological heterogeneity of AD. Rather than a disorder of protein deposition alone, AD involves neuroinflammation, immune imbalance, metabolic disturbance, extracellular matrix remodeling, and altered intercellular communication[7, 8]. Clarifying these mechanisms is therefore essential for improving early diagnosis and identifying new therapeutic opportunities.

Matrix stiffness (MS) describes the rigidity or elasticity of the extracellular matrix (ECM) surrounding cells[9]. This biomechanical property influences proliferation, differentiation, migration, and signal transduction, thereby shaping tissue development, repair, and disease processes[10, 11]. Earlier MS research has largely addressed cancer and fibrosis, in which altered matrix mechanics drive cellular remodeling and inflammatory activation[12, 13]. More recent studies indicate that MS also contributes to disorders of the central nervous system[14]. Within neural tissue, ECM mechanical changes may regulate glial reactivity and neuroinflammatory signaling through integrin-dependent mechanotransduction and cytoskeletal remodeling[15, 16]. In AD, multiple sclerosis, and related neurodegenerative diseases, the mechanical and inflammatory features of the neural microenvironment are markedly altered, with potential consequences for glial activation and immune regulation[17]. Abnormal matrix stiffening has also been linked to neuroinflammation, ECM remodeling, and impaired neuronal homeostasis during disease progression[18]. Nevertheless, the relationship between MS-related genes and AD has not been fully characterized. It also remains unclear whether matrix stiffness-related genes (MSRGs) mainly influence AD through glial mechanotransduction, mitochondrial stress, or neuroimmune remodeling.

Here, we filtered AD transcriptomic datasets to extract MSRGs-overlapping expression signatures to identify diagnostic biomarkers related to matrix stiffness using a comprehensive bioinformatics framework. Molecular regulatory network analysis, functional enrichment, and immune infiltration evaluation were then used to characterize the biological relevance and potential clinical implications of these biomarkers. Single-cell RNA sequencing (scRNA-seq) was further applied to annotate cell populations and identify disease-associated key cells. By combining cell-cell communication analysis with pseudotime trajectory inference, we examined biomarker expression and regulatory behavior within relevant cellular subsets. This work offers a mechanobiological framework for understanding AD pathology and provides theoretical support for therapeutic strategies targeting ECM mechanical microenvironment remodeling.

2. Materials and methods

2.1 Data sources

AD-related transcriptomic data were obtained from the GEO database (https://www.ncbi.nlm.nih.gov/geo/). Three datasets were included. GSE44770 (GPL4372), containing brain tissue transcriptomes from 129 AD patients and 101 controls(prefrontal cortex, visual cortex and cerebellum), was used as the training set for DEG identification. GSE5281 (GPL570), comprising 87 AD and 74 control brain tissue samples, served as the validation set for biomarker confirmation (entorhinal cortex, hippocampus, medial temporal gyrus, posterior cingulate, superior frontal gyrus and primary visual cortex). GSE175814 (GPL24676), which included single-cell transcriptomic profiles from 2 AD and 2 control human brain tissue samples(three regions: BA41/42, BA6/8, and anterior hippocampal cortex), was used to identify

key cell populations, and no samples were excluded. GSE138260 (GPL13497), comprising 17 AD and 19 control brain tissue samples, served as an independent external validation set and was not used at any stage of candidate gene selection. These datasets were used as independent validation cohorts to assess cross-dataset reproducibility across different brain regions and populations. In addition, 1,417 MSRGs were collected from the literature [19] and accessed on April 1, 2026 (Table S1).

2.2 Acquisition of candidate genes

DEGs between AD and control samples were screened in the training set using the "limma" R package (v3.58.1)[20]. The thresholds were $|\log_2 \text{fold change (FC)}| > 0.25$ and P-value < 0.05, and genes meeting these criteria were defined as DEGs. Volcano plots were generated with the "ggplot2" R package (v3.5.1)[21]. The top 10 upregulated and top 10 downregulated DEGs (ranked by $|\log_2 FC|$) are shown for visualization purposes. Heatmaps of the 10 most upregulated and 10 most downregulated genes across samples were drawn using the "ComplexHeatmap" R package (v2.21.1)[22]. Candidate genes were then obtained by intersecting DEGs with MSRGs in a Venn diagram generated by the "ggvenn" R package (v1.2.2)[23].

2.3 Functional analysis of candidate genes

GO and KEGG enrichment analyses were conducted to investigate the biological functions and signaling pathways associated with candidate genes in AD. These analyses were performed with the "clusterProfiler" R package (v4.8.3)[24]. using the whole transcriptome as the background gene set. GO terms were assessed across BP, CC, and MF categories, and BH-adjusted P (FDR) < 0.05 was used as the significance cutoff for GO and KEGG analysis. To characterize protein-level interactions, candidate gene-encoded proteins were submitted to the STRING database

(http://string-db.org). A Protein-Protein Interaction (PPI) network was constructed using a confidence score threshold of ≥ 0.4.

2.4 Machine learning analysis identifies candidate biomarkers

Machine-learning approaches were used to narrow the characteristic genes and select candidate AD biomarkers. In the training set (GSE44770), LASSO feature selection was performed between AD and control groups with the "glmnet" R package (v4.1.8)[25], using alpha = 1 and nfold = 5. Pairwise Spearman correlations were calculated among the LASSO-selected genes. The RF model was built with the "randomForest" R package (v4.7-1.1)[26]. SVM-RFE was applied using the "caret" R package (v6.0-94)[27], and five-fold cross-validation was used to evaluate the classification performance of selected gene combinations. Elastic Net sensitivity analysis ($\alpha = 0.5$, binomial logistic regression, five-fold cross-validation, $\lambda = \lambda\min$) was performed on the same samples and candidate genes. Intersections among the gene sets generated by these algorithms were displayed using the "ggvenn" R package (v1.2.2)[28] and were defined as candidate biomarkers. Biomarkers were further screened by comparing candidate biomarker expression between AD and control groups in both training and validation datasets using the Wilcoxon rank-sum test ($P < 0.05$). Genes with significant differential expression and consistent trends in both datasets were retained as biomarkers. To evaluate individual discriminative performance, ROC analysis was performed using normalized expression as continuous predictors and AD/control status as the outcome (pROC v1.18.5). AUCs and 95% CIs were calculated using the DeLong method.

2.5 Construction and validation of the nomogram model

A nomogram was constructed with the "rms" R package (v6.5-0)[29] to evaluate the predictive

value of all biomarkers for AD in training-set AD and control samples (GSE44770). Model calibration was assessed by calibration curves generated with the same package; a slope close to 1 indicated better agreement between predicted and observed probabilities. A Hosmer-Lemeshow (HL) $P > 0.05$ was considered evidence of acceptable calibration. The "pROC" R package (v1.18.5)[30] was used for ROC analysis, and the AUC was calculated, with $AUC > 0.7$ indicating predictive value.

2.6 Molecular regulatory network analysis

To examine biomarker-miRNA relationships, biomarker-associated miRNAs were obtained from the StarBase (v3.0) database (https://starbase.sysu.edu.cn/), and only miRNAs with pancancerNum > 6 were retained. TFs potentially interacting with biomarkers at the transcriptional level were identified using the Transcriptional Regulatory Relationships Unraveled by Sentence-based Text mining (TRRUST) database (http://www.grnpedia.org/trrust).

2.7 Gene set enrichment analysis (GSEA)

Biomarker-related pathways and biological processes in AD were examined by GSEA. The c2.cp.kegg.v7.5.1.symbols.gmt gene set was downloaded from the MSigDB (https://www.gsea-msigdb.org/gsea/msigdb/) and used as the reference set. In the training set (GSE44770), Spearman correlation coefficients between each biomarker and all other genes were calculated with the "cor" function in the "stats" R package (v4.2.2)[31]. Genes were ordered from highest to lowest correlation coefficient, and pathway enrichment was performed with the "clusterProfiler" R package (4.8.3), with $P < 0.05$ as the threshold.

2.8 Subcellular localization

For subcellular localization prediction, amino acid sequences of proteins encoded by the biomarkers were downloaded from the NCBI database (https://www.ncbi.nlm.nih.gov/). Sequence completeness and accuracy were checked before submission to the Wolf Proteome Localization Prediction by WoLF PSORT (WoLF PSORT) database (https://wolfpsort.hgc.jp/). Localization information reported by this platform was then recorded.

2.9 Immune infiltration analysis

Immune-cell infiltration in AD and normal samples was estimated in the training dataset with the "CIBERSORT" R package (v0.1.0)[32], which quantified the relative abundance of 22 immune cell types. Samples with $P > 0.05$ were removed. The Wilcoxon test was used to compare infiltration differences between groups, and $P < 0.05$ was set as the significance threshold. Immune cells with significant abundance differences were considered differential immune cells. Spearman analysis was then used to assess correlations between biomarkers and differential immune infiltrating cells, as well as correlations among differential immune cells ($|cor| > 0.3$ and $P < 0.05$).

2.10 Single-cell sequencing

The GSE175814 dataset was analyzed with the "Seurat" R package (v 5.1.0)[33]. Quality control excluded genes expressed in fewer than 3 cells, cells with fewer than 200 or more than 10,000 detected genes (nFeature_RNA), cells with mitochondrial transcript proportions (percent.MT) > 15%, possible doublets, and cells with total UMI counts (nCount_RNA) below 200 or above 30,000. Data were log-normalized with NormalizeData, and highly variable genes were selected with FindVariableFeatures. After ScaleData normalization, principal component analysis (PCA) was conducted on the highly variable genes. Significant principal components

were evaluated by the JackStraw permutation test ($P < 0.05$), and the ElbowPlot was used to guide component selection. Batch effects were corrected using Harmony. Cell clustering was then performed with FindClusters across resolution values from 0.1 to 1, and clustree was used to visualize clustering stability. After a resolution was selected, DimPlot generated the UMAP visualization. A stacked bar plot summarized the cell number of each sample. In GSE175814, the chi-square test compared cell-type proportions between groups ($P < 0.05$), and the Wilcoxon test assessed biomarker expression ($P < 0.05$) to identify key cells.

2.11 Functional enrichment, differentiation trajectory, and cell-cell communication analysis

Reactome GSVA analysis was applied to characterize biological pathways and functions across different cell types in AD. Reactome metabolic pathway data were retrieved using the "AnnotationDbi" R package (v1.64.1)[34], and cell-type-specific enrichment was assessed with the "GSVA" R package (v1.50.0)[35]. Pathways containing fewer than 10 or more than 500 genes were excluded to reduce excessive noise or overly broad signals, and GSVA scores (enrichment scores, ES) were generated. For key cells, secondary clustering was performed at resolution = 0.2. Cell trajectory and pseudotime analyses were then conducted on key cell clusters using the "monocle" package (v 2.26.0)[36]. The plot_genes_in_pseudotime function was used to display biomarker expression across pseudotime stages, thereby showing changes during cell differentiation.

Cell-cell communication among all annotated cell types, as well as between key cells and other cell types, was analyzed in GSE175814 with the "CellChat" R package (v1.6.1)[37]. Potential ligand-receptor interactions were inferred to estimate communication signals among cell populations, using $P < 0.05$ and log2mean ≥ 0.1 as cutoffs. Communication networks were

visualized with the "netVisual_circle" function.

2.12 Statistical analysis

Bioinformatics analyses were conducted in R software (v4.3.1). Between-group comparisons were evaluated with the Wilcoxon test, and $P < 0.05$ was considered statistically significant.

3. Results

3.1 Identification of candidate genes associated with MSRGs in AD

In GSE44770, differential expression analysis compared AD brain tissue samples with control brain tissue samples. This analysis identified 509 DEGs, including 293 genes that were upregulated and 216 genes that were downregulated in the AD group. A volcano plot was generated for these DEGs. Based on log2FC ranking, CRH, RPS4Y1, and other genes were among the top ten downregulated genes, whereas S100A8, SERPINA3, and others were among the top ten upregulated genes in AD (Fig. 1A). Figure 1B shows the top 10 upregulated and top 10 downregulated DEGs (ranked by $|\log_2 FC|$) for illustrative purposes; the full DEG list meeting the significance threshold is provided in Table S2. Intersecting DEGs (n = 509) with MSRGs (n = 1,417) yielded 81 candidate genes (Fig. 1C) (Table S3).

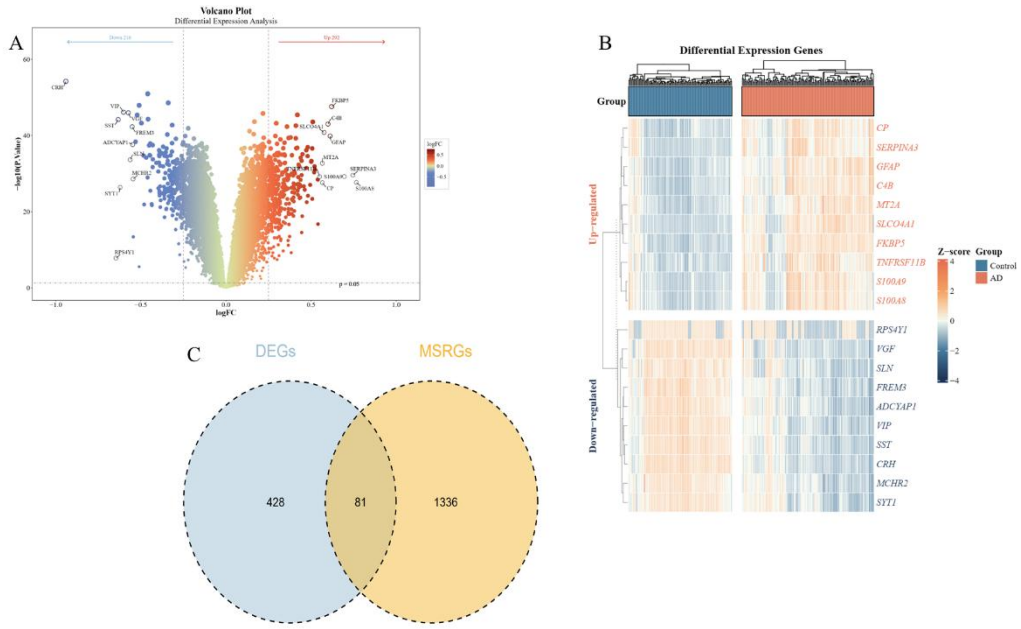


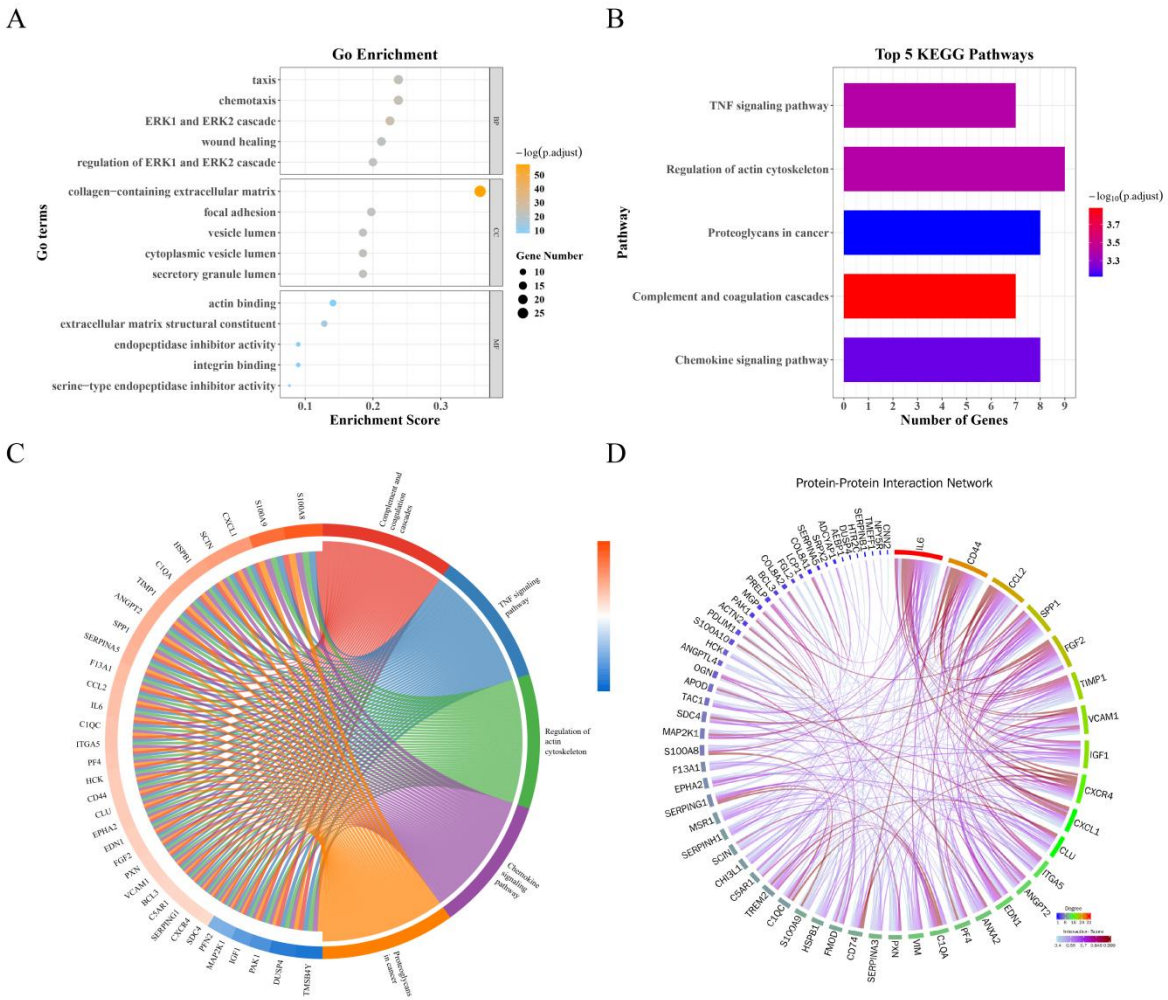
Figure. 1 Identification of candidate genes. (A) Volcano plot of 509 DEGs, including 293 upregulated and 216 downregulated genes, in AD samples compared with control samples. (B) Heatmap showing the top 10 most significantly upregulated and downregulated genes in AD group samples. Orange indicates high expression of the gene in a specific sample, while blue indicates low expression. (C) Venn diagram of DEGs and MSRGs.

3.2 Exploration of the biological functions of candidate genes

GO enrichment analysis of candidate genes identified 729 significant terms (FDR < 0.05), including 641 BP terms, 40 CC terms, and 48 MF terms (P < 0.05) (Fig. 2A). The five leading BP terms were taxis, chemotaxis, ERK1 and ERK2 cascade, wound healing, and regulation of ERK1 and ERK2 cascade. The five leading CC terms included collagen-containing extracellular matrix, focal adhesion, vesicle lumen, cytoplasmic vesicle lumen, and secretory granule lumen. The five leading MF terms were actin binding, extracellular matrix structural constituent, endopeptidase inhibitor activity, integrin binding, and serine-type endopeptidase inhibitor activity. KEGG analysis identified 52 significant pathways (FDR < 0.05), including

chemokine signaling pathway and complement and coagulation cascades (Fig. 2B). The chord diagram displayed the relationships between candidate genes and enriched pathways (Fig. 2C). Detailed GO and KEGG results with nominal P and corresponding FDR values are provided in Table S4 and Table S5. These findings indicate that protein regulation is closely connected with signal transduction pathways and AD-related pathology.

The PPI network contained 63 gene-encoded proteins and 282 interaction relationships (Fig. 2D). Within this network, inflammation-related genes, such as S100A8, S100A9, and SERPINA3, and ECM-associated genes, including COL8A1, COL8A2, and OGN, formed dense interaction clusters. These patterns suggest that candidate genes are mainly involved in inflammatory responses and ECM remodeling during AD progression. Thus, MSRGs may contribute to AD through coordinated involvement in multiple pathological pathways rather than acting independently.



253

254 **Figure. 2** Exploration of the biological functions of candidate genes. (A) GO enrichment

255 analysis entry chart of candidate genes. (B) KEGG enrichment analysis entry chart of candidate

256 genes. (C) Chord diagram of KEGG enrichment analysis of candidate genes. (D) PPI network

257 of candidate gene-encoded proteins.

258 3.3 Identification of FREM3, DUSP4, and FAM107A as biomarkers for AD

259 LASSO feature selection, RF, and SVM-RFE were applied to candidate genes to identify AD-

260 associated characteristic genes and improve model performance. LASSO selected features at a

261 lambda value of 0.0286 and identified eight characteristic genes: FREM3, DUSP4, CHI3L1,

262 AEBP1, IGF1, FAM107A, PRELP, and CLU (Fig. 3A,B). RF ranked IGF1, HSPB1, FREM3,

263 FAM107A, DUSP4, PAK1, SERPING1, CBLN4, LCP1, and S100A10 as the top 10

characteristic genes (Fig. 3C,D). SVM-RFE selected 18 characteristic genes (Fig. 3E,F; Table S6). Intersecting the three feature sets produced four overlapping genes, FREM3, IGF1, DUSP4, and FAM107A, which were defined as candidate biomarkers (Fig. 3G). The eight LASSO-selected genes showed moderate-to-strong correlations (maximum $\rho = 0.89$, FREM3–IGF1; Fig. S1A). Elastic Net retained all eight genes, including all three final biomarkers (100% retention), supporting robustness across regularization methods (Fig. S1B, C)

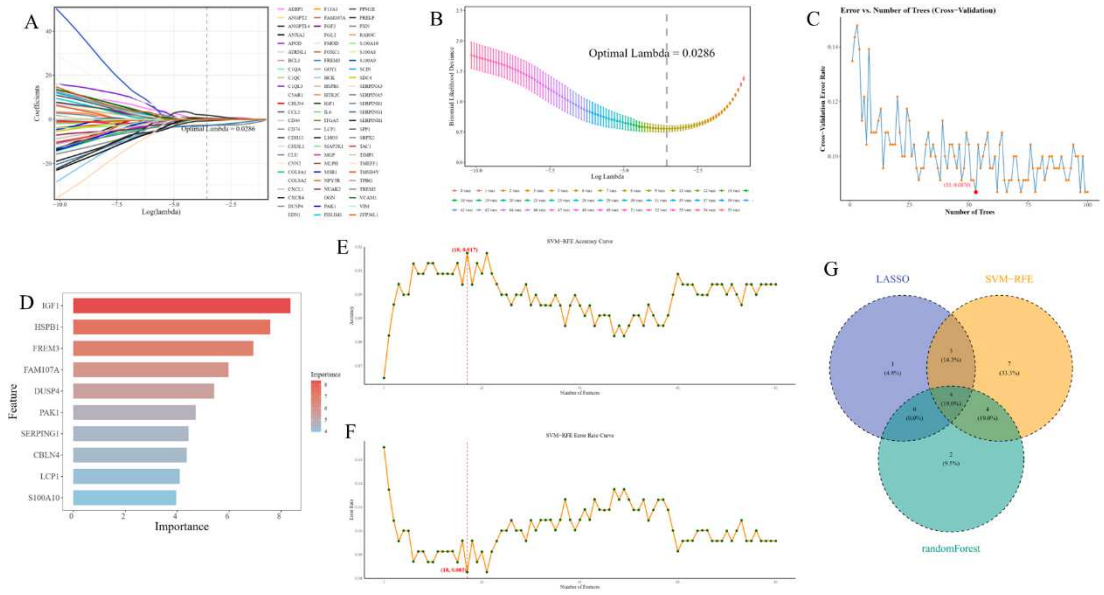


Figure. 3 Identification of key genes. (A)LASSO regression path plot. (B) LASSO regression cross-validation curve. (C, D) Random Forest model and selected feature genes. (E, F) SVM-RFE analysis. (G) Venn diagram of the three gene sets.

3.4 Expression validation and discriminative performance of biomarkers

Candidate biomarker expression was evaluated in both GSE44770 and GSE5281. FREM3, DUSP4, and FAM107A showed significant differences with concordant expression trends in the two datasets; consequently, these genes were identified as biomarkers ($P < 0.05$) (Fig. 4A,B). Individual ROC analysis showed AUCs of 0.947 (95% CI: 0.920–0.973), 0.938 (0.905–0.972),

and 0.936 (0.905–0.966) for FREM3, DUSP4, and FAM107A, respectively, in GSE44770 (Fig. 4C), versus 0.637 (0.548–0.726), 0.750 (0.672–0.828), and 0.627 (0.541–0.713) in GSE5281 (Fig. 4D).

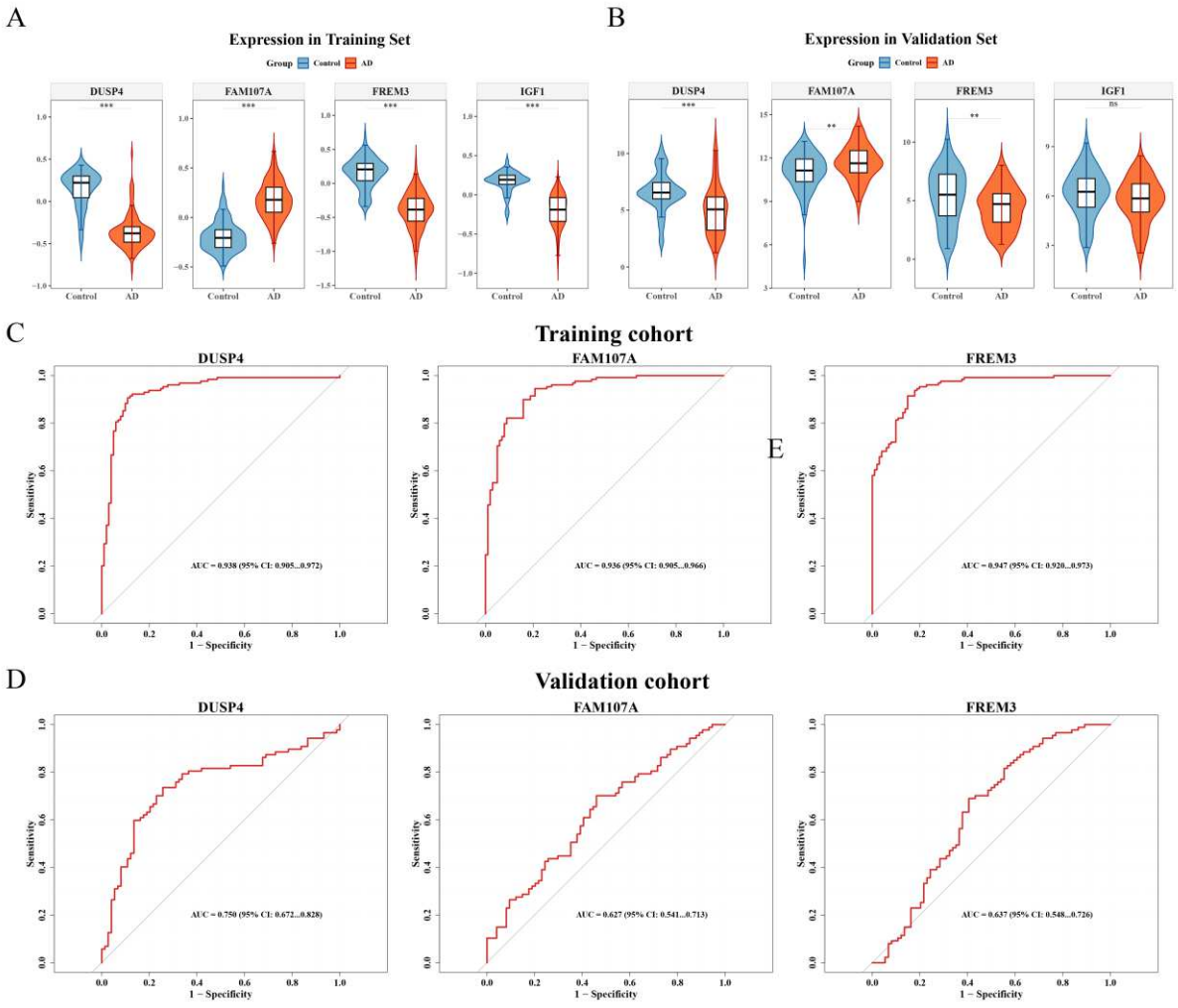


Figure. 4 Expression levels and discriminative performance of key genes. (A) Expression levels of key genes in the training set. (B) Expression levels of key genes in the validation set. *P < 0.05; **P < 0.01; ***P < 0.001; ****P < 0.0001 (Wilcoxon rank-sum test). (C) Individual ROC curves for FREM3, DUSP4, and FAM107A in GSE44770. (D) Individual ROC curves for the three biomarkers in GSE5281. AUC values with 95% confidence intervals (DeLong method) are shown for each gene.

3.5 Biomarkers demonstrate excellent predictive value for AD

A nomogram based on biomarker expression values was used to estimate AD risk. When the total score was 180 points, the predicted AD probability reached 0.706, indicating a relatively high estimated risk according to the model (Fig. 5A). Calibration and ROC analyses were then used to assess model performance. The H-L test in the calibration curve yielded P = 0.528, showing no significant difference between predicted and observed probabilities and indicating good model fit (Fig. 5B). ROC analysis showed an AUC of 0.963 (training set, GSE44770), demonstrating excellent classification accuracy for the nomogram (Fig. 5C). Applied without refitting to GSE5281, the model yielded an AUC of 0.756 (95% CI: 0.681–0.831), with 65.5% sensitivity, 74.3% specificity, and 69.6% accuracy (Fig. 5D). In the independent GSE138260 (n = 36), AUC was 0.604 (95% CI: 0.412–0.796), with 88.2% sensitivity, 42.1% specificity, and 63.9% accuracy(Fig. 5E); the wide CI reflects the small sample size.

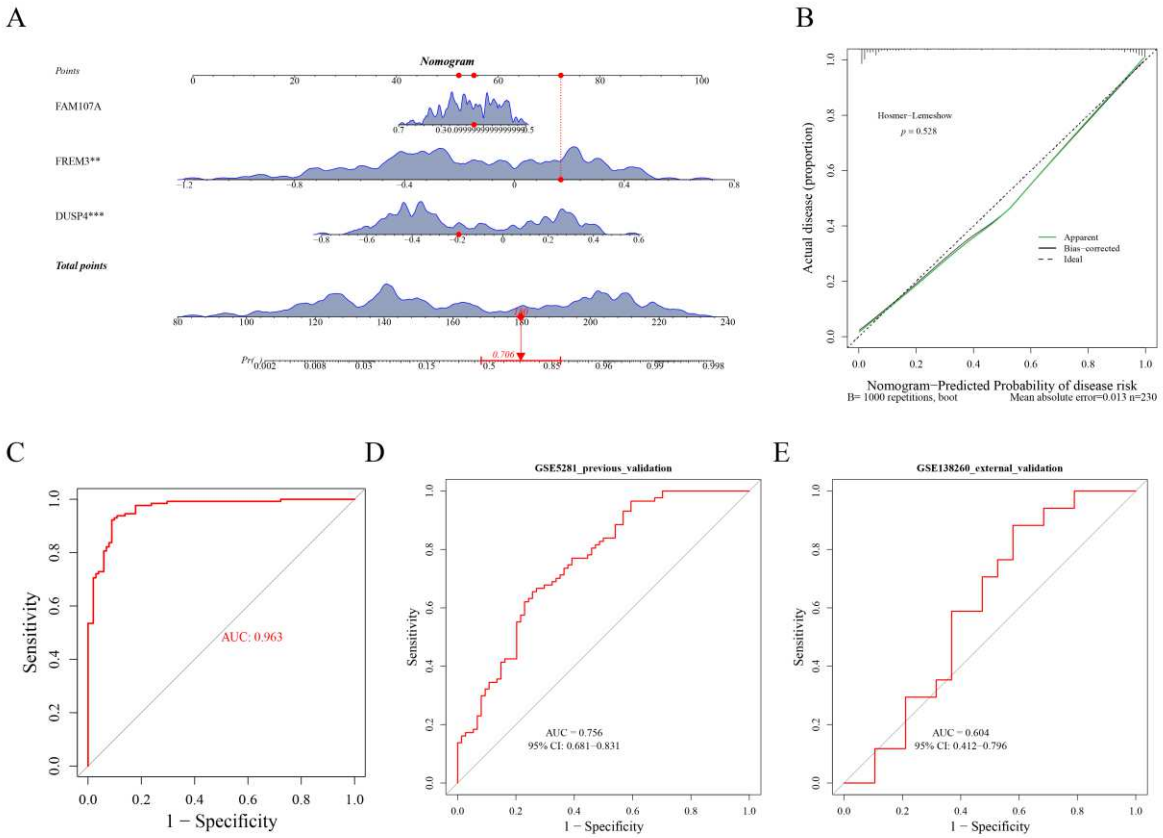


Figure. 5 The Predictive Value of Biomarkers for AD. (A) Nomogram for AD prediction based on biomarkers. (B) Calibration curve. (C) ROC curve of the nomogram in the training set (GSE44770; AUC = 0.963). (D) ROC curve in GSE5281, showing an AUC of 0.756 (95% CI: 0.681–0.831. (E) ROC curve in the external GSE138260 cohort (n = 36), showing an AUC of 0.604 (95% CI: 0.412–0.796).

3.6 Biological information of biomarkers

Molecular regulatory network analysis predicted 26 miRNAs for DUSP4 and 10 miRNAs for FAM107A, whereas no miRNA was predicted for FREM3. Five miRNAs, hsa-miR-193a-5p, hsa-miR-194-3p, hsa-miR-4727-5p, hsa-miR-5001-3p, and hsa-miR-615-5p, were shared by two biomarkers. After duplicate entries were removed, 31 miRNAs remained for network visualization (Fig. 6A; Table S7). The network suggested that hsa-let-7b-5p may target both DUSP4 and FAM107A. This interaction may influence the MAPK signaling pathway and

neuronal apoptosis during AD progression through coordinated post-transcriptional regulation. At the transcriptional level, TFs were predicted to interact with biomarkers. Four TFs were predicted for FAM107A, two for FREM3, and five for DUSP4, giving 11 TFs in total. These TFs were displayed in the regulatory network (Fig. 6B; Table S8). FAM107A was regulated by GATA2, CREB1, FOXC1, and NFKB1, whereas FREM3 was regulated by YY1 and FOXL1. The network also indicated that E2F1 and E2F6 may jointly regulate DUSP4 expression, potentially affecting cell cycle progression and neuronal survival through an E2F-mediated transcriptional axis in AD.

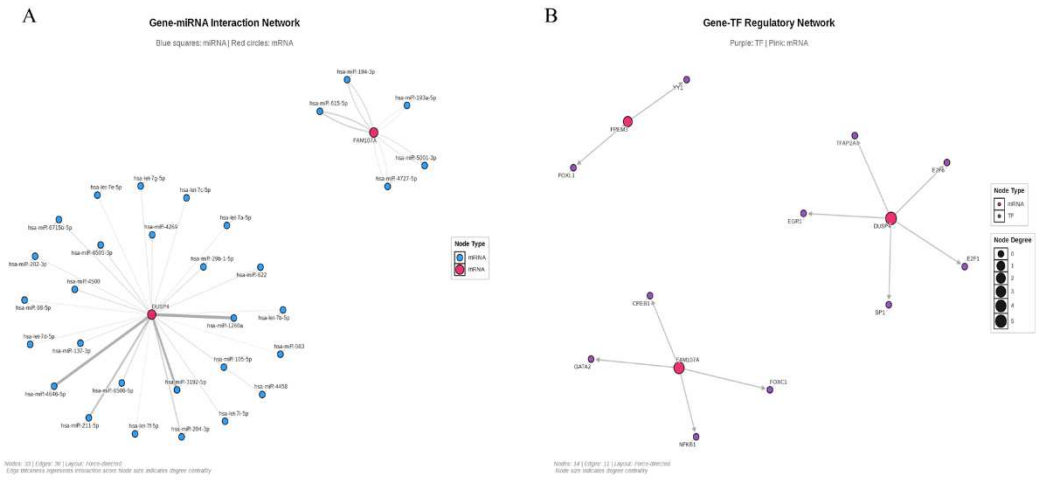


Figure. 6 Molecular Network Regulation Analysis of Biomarkers. (A) miRNA-mRNA regulatory network containing 33 nodes and 36 edges. (B) TF-mRNA regulatory network containing 14 nodes and 11 edges.

3.7 GSEA enrichment analysis of three biomarkers

GSEA identified 71 pathways enriched for DUSP4 (Table S9), including Oxidative phosphorylation (Fig. 7A). FAM107A was enriched in 65 pathways (Table S10), including

Ribosome (Fig. 7B). FREM3 was enriched in 64 pathways (Table S11), including Cytokine-cytokine receptor interaction (Fig. 7C). All three biomarkers were jointly enriched in 55 pathways (Table S12), including Oxidative phosphorylation and Ribosome (Fig. 7D). In most pathways, DUSP4 and FREM3 displayed similar expression patterns, whereas FAM107A showed the opposite trend, suggesting that DUSP4 and FREM3 may have closer biological and functional similarity.

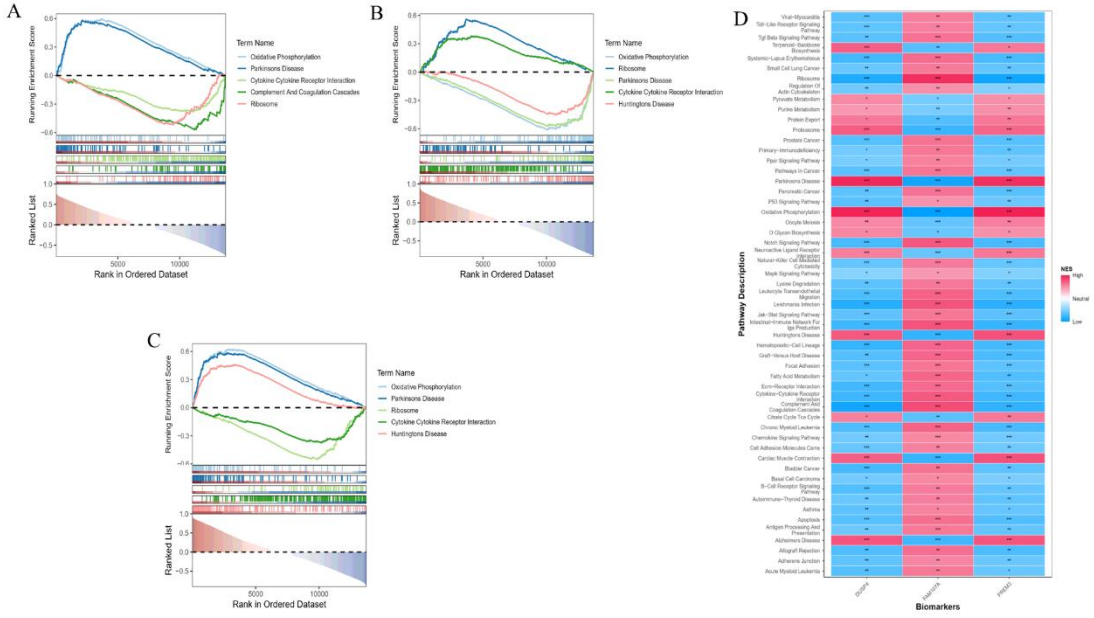


Figure. 7 GSEA analysis. (A) GSEA enrichment analysis of DUSP4. The top 5 pathways ranked by P value from smallest to largest were: Oxidative phosphorylation, Parkinson's disease, Cytokine-cytokine receptor interaction, Complement and coagulation cascades, and Ribosome. (B) GSEA enrichment analysis of FAM107A. The top 5 pathways ranked by P-value from smallest to largest were: Oxidative phosphorylation, Ribosome, Parkinson's disease, Cytokine-cytokine receptor interaction, and Huntington's disease. (C) GSEA enrichment analysis of FREM3. The top 5 pathways ranked by P-value from smallest to largest were: Oxidative phosphorylation, Parkinson's disease, Ribosome, Cytokine-cytokine receptor interaction, and

Huntington's disease. (D) Enrichment pathway correlation heatmap.

3.8 Subcellular localization of biomarkers

Subcellular localization prediction indicated that all three biomarkers might localize to the nucleus (Fig. 8). Additional predicted distributions differed among markers. DUSP4 showed notable plasma membrane localization and modest mitochondrial localization. FREM3 was mainly cytoplasmic, with extracellular and endoplasmic reticulum localization consistent with its secretory function and minor Golgi localization related to secretory processing. FAM107A showed prominent cytoplasmic and mitochondrial accumulation, suggesting involvement in cytoplasmic signaling and mitochondrial homeostasis; minor lysosomal and plasma membrane localization also suggested a possible role in intracellular trafficking.

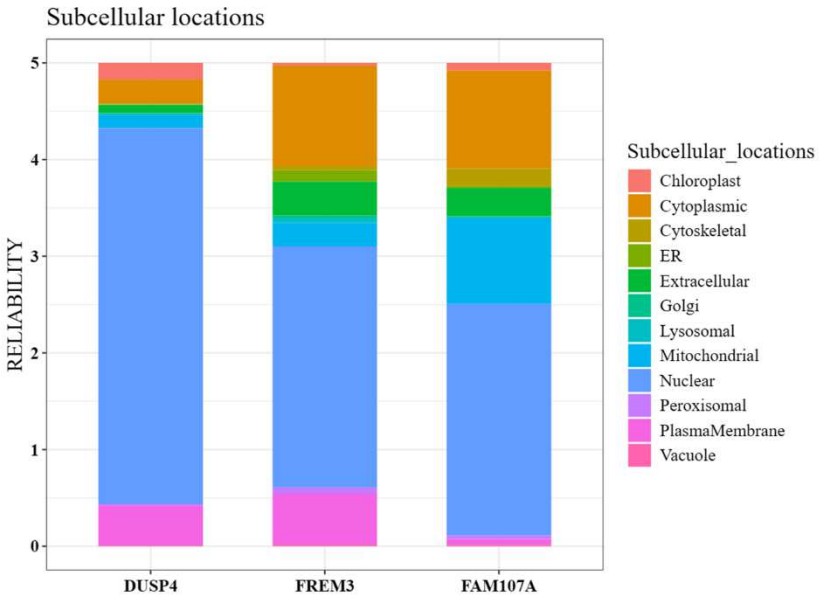


Figure. 8 Bar chart of biomarker gene subcellular localization results.

3.9 Immune infiltration analysis

Immune infiltration analysis suggested that the immune microenvironment was associated with AD diagnosis. The enrichment scores of different immune cells across samples are shown in

Fig. 9A,B, and 13 immune cell types differed significantly between groups. Violin plots confirmed distinct immune infiltration patterns, using $P < 0.05$ as the significance threshold. Correlation analysis showed that DUSP4 and FREM3 were positively correlated with CD8 T cells (cor = 0.53, $P < 0.05$; cor = 0.65, $P < 0.05$, respectively) and plasma cells (cor = 0.60, $P < 0.05$; cor = 0.57, $P < 0.05$, respectively). FAM107A was positively correlated with resting Natural Killer (NK) cells (cor = 0.54, $P < 0.05$). Activated CD4 memory T cells were positively correlated with CD8 T cells (cor = 0.45, $P < 0.05$), and resting NK cells were positively correlated with resting CD4 memory T cells (cor = 0.33, $P < 0.05$). In contrast, resting CD4 memory T cells were negatively correlated with CD8 T cells (cor = -0.51, $P < 0.05$) (Fig. 9C).

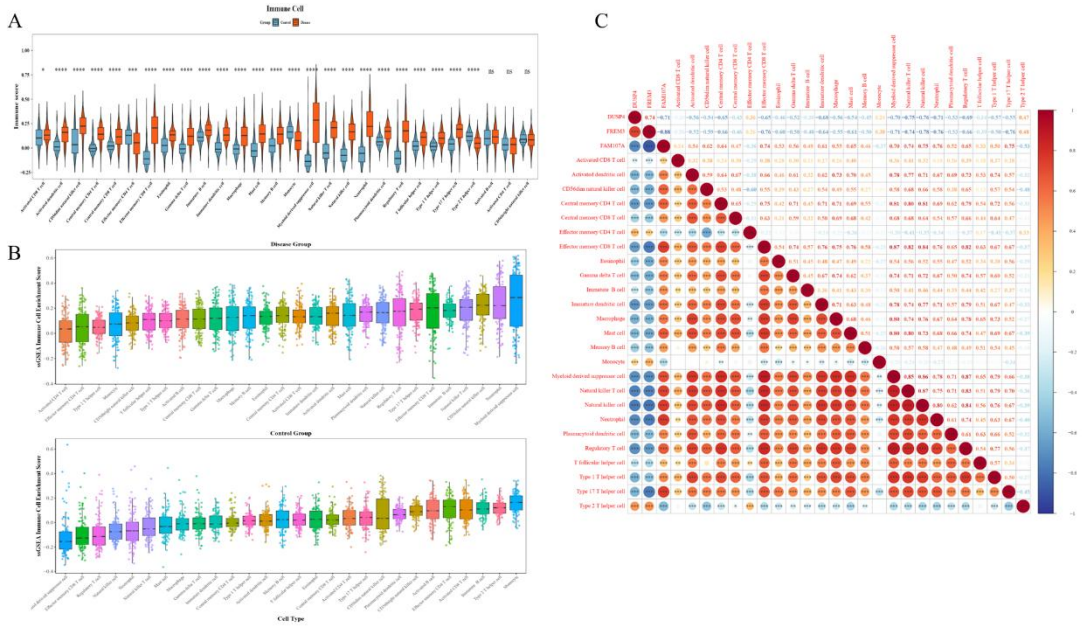


Figure. 9 Immune infiltration analysis. (A) Immune scores of 28 immune cell types in the two groups. (B) Immune enrichment scores of 28 immune cell types in the two groups. (C) Differential immune cell correlation matrix plot.

3.10 Single-cell sequencing analysis

Before quality control, the dataset included 28,759 cells and 28,104 genes. After filtering,

26,468 cells and 28,104 genes were retained for downstream analysis (Fig. 10A,B). A scatter plot comparing RNA features with RNA counts showed a strong positive linear relationship, indicating satisfactory quality control for the single-cell dataset (Fig. 10C). Highly variable genes were then selected, and the top 2,000 genes were prioritized for analysis. The 10 genes with the largest variation, including FLT1 and RELN, were labeled (Fig. 10D). The first 15 PCs were used for subsequent clustering (Fig. 10E,F). A resolution of 0.6 was finally selected, resulting in 22 cell clusters (Fig. 10G,H).

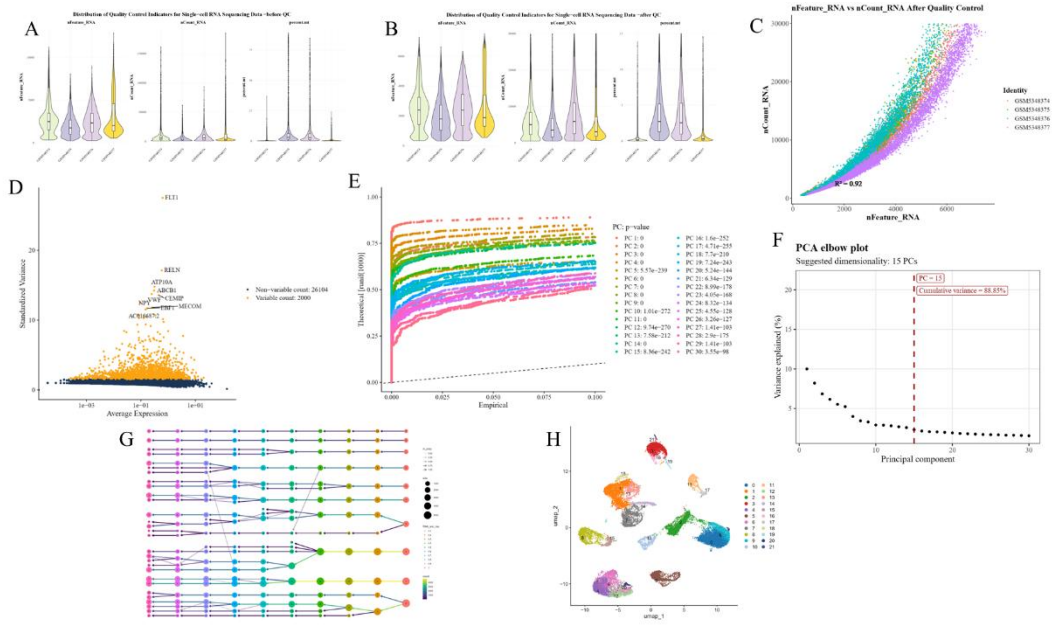


Figure. 10 Single-cell data processing. (A) Single-cell data before quality control. (B) Single-cell data after quality control. (C) Correlation between nFeature RNA and nCount RNA after quality control. (D) Filter highly variable genes. (E) PCA Permutation Test Plot. (F) Principal Component Scatter Plot. (G) Single-cell resolution clustering tree diagram. (H) UMAP plot of cell cluster classification.

3.11 Cell clustering, annotation, and proportion analysis

After annotation, the expression distribution of marker genes across different cell types was

displayed (Table 1) (Fig. 11A). UMAP dimensionality reduction was used to classify cell clusters, and 10 cell types were annotated, including Oligodendrocyte, Neuron, and other populations (Fig. 11B). A stacked bar chart quantified the cell composition of AD and control samples, and group differences in cell proportions were also summarized (Fig. 11C,D).

Table 1. Characteristic gene information corresponding to each cell type.

No.	Celltype	Marker gene
1	Oligodendrocyte	MYRF, MOG, ASPA, FA2H
2	Neuron	LINC00507, PDGFD, LHX6, NXPH1
3	Neutrophil	FLT1, VWF, CLDN5, NOSTRIN, CDH5
4	Astrocyte	SLCO1C1, SLC14A1, BMPR1B, F3
5	Endothelial cell	HLA-DMB, CIITA, CSF1R
6	T cell	TNC, PAX6
7	Glial progenitor	C1QC, CX3CR1, TAL1, HLA-DQB1, LILRB4
8	Microglial cell	GLI3, SLC1A2, SPON1, WIF1
9	Fibroblast	LHFPL3, MEGF11, GPR17, MYT1
10	Macrophage	IL1RAPL2','TSHZ2','SCHLAP1','OTOGL'

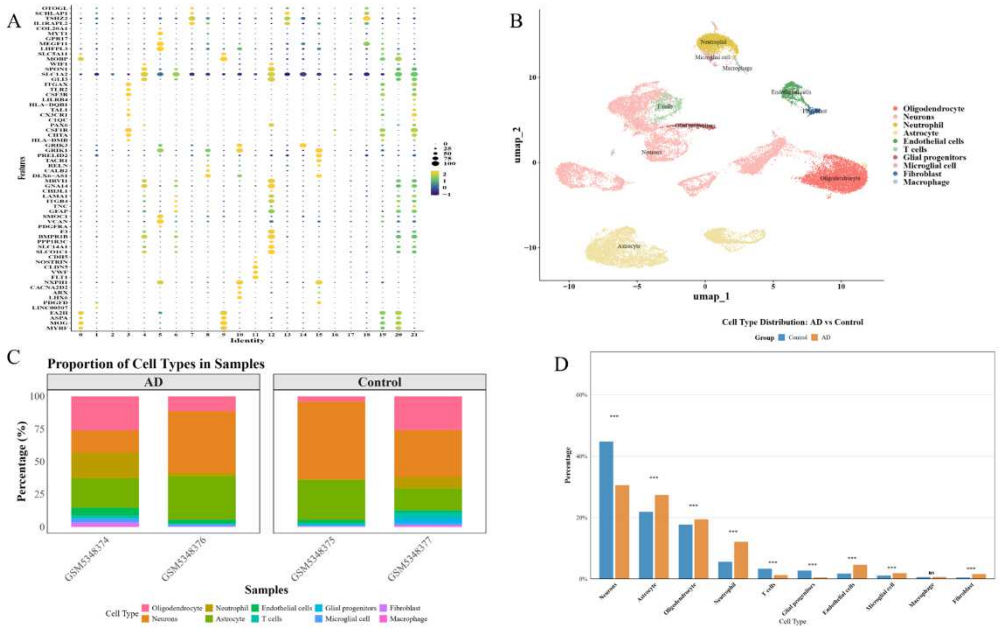


Figure. 11 Characteristic gene information corresponding to each cell type. (A) Bubble plot of marker gene expression in various cell types. (B) UMAP visualization of cell clusters in the dataset GSE175814. (C) Stacked chart of the proportion of various cell clusters. (D) Differences in the cell proportions between the AD group and the control group. (Asterisks indicate significance: *P < 0.05, **P < 0.01, ***P < 0.001, ****P < 0.0001; ns, not significant)

3.12 Identification of key cells, pathway enrichment, and astrocyte differentiation trajectory

In the single-cell dataset, cell-type proportions were compared between AD patients and normal controls using the chi-square test (P < 0.05). Except for macrophages, the other nine cell types differed significantly in proportion between groups (Fig. 12A). Expression comparison of the three biomarkers across cell clusters showed that astrocytes expressed all three biomarkers significantly (P < 0.05), so astrocytes were defined as the key cell type (Fig. 12B). Reactome GSVA analysis of all annotated cell types revealed cell-type-specific pathway enrichment. The activation pathway of Na+ permeable kainate receptors was highly enriched in fibroblasts, endothelial cells, and microglial cells (Fig. 12C). Pseudotime analysis was then performed for

astrocytes. The first 12 principal components were selected by principal component analysis (Fig. 12D,E), and secondary clustering at resolution = 0.2 identified 10 astrocyte subclusters (Fig. 12F). The differentiation trajectory showed that astrocytes from the AD group were concentrated in early differentiation stages, whereas astrocytes from controls were more enriched in middle and late stages (Fig. 12G). For biomarker dynamics, DUSP4 and FREM3 showed a “low-high-low” trajectory, while FAM107A increased continuously from a low level (Fig. 12H). These results suggest that astrocyte differentiation is altered in AD and may involve early-stage accumulation or delayed maturation. The dynamic patterns of DUSP4, FREM3, and FAM107A also indicate possible stage-specific regulatory roles during astrocyte differentiation in AD.

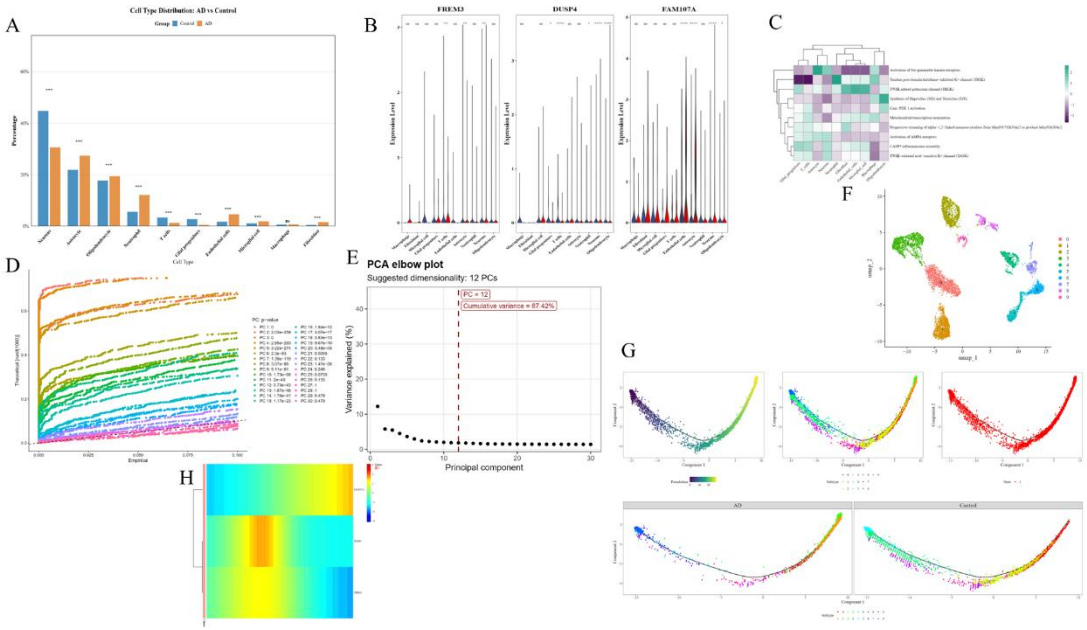


Figure. 12 Single-cell atlas, pathway enrichment, and astrocyte differentiation trajectory in AD. (A) Bar plot showing the proportion of each cell type in AD patients and normal controls. (B) Expression levels of three biomarkers across different cell clusters. (C) Reactome-based GSVA enrichment analysis. (D, E) Principal component analysis (PCA) of astrocytes. (F) Clustering

of astrocytes. (G) Pseudotime trajectory analysis of astrocyte differentiation. (H) Dynamic expression patterns of three biomarkers along the differentiation trajectory.

3.13 Cell communication

CellChat analysis showed that astrocytes communicated with all other cell types in both AD and control groups. However, astrocyte-T cell communication was stronger in the AD group than in controls, whereas astrocyte communication with T cells and macrophages was weaker in the control group (Fig. 13A-D). Ligand-receptor analysis indicated that the pathways with the highest communication probability in both groups were microglial cell-glial progenitor cells and microglial cell-neurons (Fig. 13E-F). These results suggest that astrocyte communication differs in AD, while microglia-mediated communication pathways remain dominant in both groups.

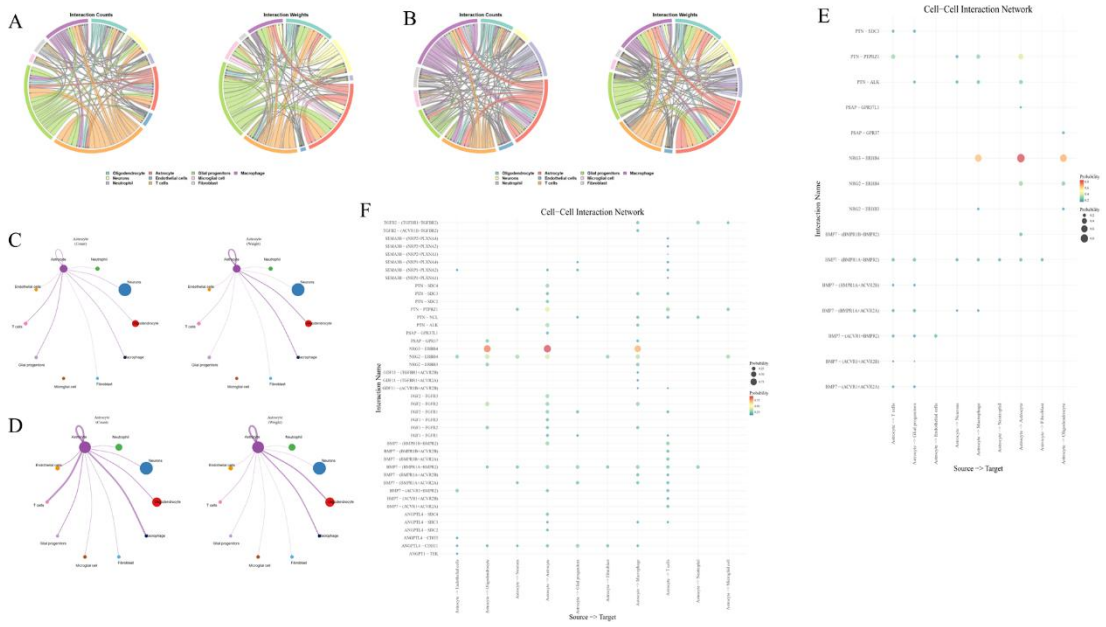


Figure. 13 Cell-cell communication analysis of astrocytes in AD. (A-D) CellChat analysis illustrating the communication network between astrocytes and other cell types (A, C: control group; B, D: AD group). (E, F) Ligand-receptor interaction analysis in the control and AD

groups.

4. Discussion

ECM remodeling and altered tissue mechanics are increasingly recognized in neurodegenerative disease, but the contribution of MSRGs to AD remains insufficiently characterized. In this study, integrated transcriptomic analysis, machine learning, immune infiltration assessment, and single-cell analysis identified FREM3, DUSP4, and FAM107A as diagnostic biomarkers related to AD. The biomarker-based nomogram reached an AUC of 0.963, indicating strong diagnostic performance. At the mechanistic level, these markers were linked to oxidative phosphorylation, inflammatory signaling, and astrocyte-associated processes, suggesting that ECM stiffness sensing may influence AD through mitochondrial dysfunction and neuroimmune remodeling.

The enrichment profile of the identified biomarkers indicates that oxidative phosphorylation and inflammatory signaling may be important downstream processes of matrix stiffness-associated changes in AD. The shared oxidative phosphorylation signal supports a link between MSRG-related mechanical remodeling and mitochondrial energy stress, which is increasingly recognized in AD-related neurodegeneration[38]. ECM stiffening is not simply a structural consequence of disease[15, 39]. It can also guide cellular behavior through integrins, focal adhesion kinase (FAK), cytoskeletal remodeling, and nucleus-cytoskeleton coupling[40, 41]. Consistent with this concept, the present functional enrichment results highlighted focal adhesion, integrin binding, and regulation of the actin cytoskeleton, all of which are core components of mechanosensing. In AD, persistent ECM stiffening may disrupt mechanosensitive signaling and thereby alter glial activation, inflammatory output, and neuronal metabolic adaptation.

These observations suggest that abnormal ECM mechanics may actively contribute to neurodegeneration rather than merely reflect secondary tissue damage.

FREM3, DUSP4, and FAM107A may connect ECM mechanical changes with AD pathology through complementary mechanisms. FREM3 belongs to the FRAS1-related ECM protein family and is involved in neuronal development, synaptic organization, and ECM interactions[42]. Dysregulated FREM3 expression has been reported in neurological disorders, suggesting a possible role in neurodegeneration. Because ECM stiffness strongly affects neuronal behavior and glial activation, altered FREM3 expression may reflect extracellular microenvironment remodeling in AD[43]. In this study, FREM3 showed the strongest positive correlation with $CD8^+$ T-cell infiltration ($r = 0.65$). This finding suggests a potential link between ECM remodeling and adaptive immune infiltration in AD. Since $CD8^+$ T-cell accumulation may contribute to neuronal injury and blood-brain barrier disruption, FREM3-associated ECM changes could participate in neuroimmune remodeling during disease progression.

DUSP4 is a dual-specificity phosphatase that negatively regulates MAPK signaling[44]. By dephosphorylating ERK1/2 and p38 MAPKs, it contributes to cellular stress responses and inflammatory regulation[45, 46]. Reduced DUSP4 expression may prolong MAPK activation, thereby enhancing oxidative stress, neuroinflammation, and neuronal apoptosis in AD[47, 48]. Sustained MAPK signaling has also been associated with amyloid-β accumulation, tau hyperphosphorylation, and synaptic dysfunction. Therefore, DUSP4 may act as a regulatory node linking stiffness-related signaling abnormalities to classical AD pathological processes. Among the three biomarkers, DUSP4 showed the broadest enrichment profile, involving 71 signaling pathways. This result further supports its role in inflammatory and metabolic

remodeling. Its association with plasma cells (r = 0.60) also suggests that MAPK dysregulation may contribute to adaptive immune activation in the AD microenvironment.

FAM107A is a stress-responsive protein with potential neuroprotective relevance[49]. Although it was initially described mainly in cancer biology[50, 51], proteomic evidence has also connected altered FAM107A abundance with neurodegenerative disease[52]. In the present analysis, FAM107A was associated with oxidative phosphorylation and ribosomal pathways, suggesting involvement in metabolic adaptation and intracellular stress control. Because mitochondrial dysfunction and proteostasis impairment are central features of AD, abnormal FAM107A expression may contribute to neuronal metabolic imbalance and progressive neurodegeneration. Along the astrocyte pseudotime trajectory, FAM107A increased continuously, indicating that it may participate in sustained metabolic adaptation and stress responses during reactive astrocyte progression.

The co-enrichment of all three biomarkers in oxidative phosphorylation emphasizes mitochondrial energy metabolism as a convergent MSRG-associated mechanism in AD. Oxidative phosphorylation is the main source of neuronal ATP, and its impairment is considered an early event in AD[38, 53]. Mitochondrial structural abnormalities, ATP depletion, and excessive reactive oxygen species accumulation can drive synaptic dysfunction and neuronal loss[54]. Within this framework, DUSP4 downregulation may strengthen oxidative stress by allowing persistent MAPK activation, whereas FREM3-related ECM remodeling may affect mechanotransduction and neuronal metabolic adaptation. FAM107A may further participate in mitochondrial stress regulation and intracellular energy homeostasis. Together,

these findings suggest that disrupted matrix stiffness sensing may promote neurodegeneration by disturbing neuronal energy metabolism, inflammatory balance, and ECM integrity.

The miRNA-TF-mRNA network indicated that FREM3, DUSP4, and FAM107A are regulated within multilayered transcriptional and post-transcriptional systems. Several predicted miRNAs targeted more than one biomarker, suggesting coordinated regulation during AD progression. TFs such as E2F1, CREB1, and NFKB1 may also regulate biomarker expression. This regulatory pattern may connect matrix stiffness-associated signaling with neuronal survival and inflammatory activation.

The predicted nuclear localization of all three biomarkers was another noteworthy observation. MSRGs are typically considered ECM proteins, adhesion-related molecules, or membrane-associated mechanosensors[55]. Therefore, the predicted nuclear localization of FREM3, DUSP4, and FAM107A may indicate functions beyond extracellular remodeling. DUSP4 and FAM107A have known links to intracellular signaling and transcriptional regulation, whereas the biological meaning of nuclear FREM3, an ECM-associated protein, remains uncertain and should be interpreted cautiously. Mechanotransduction can influence nuclear architecture and gene expression through cytoskeleton-nucleus coupling, raising the possibility that these biomarkers participate in cellular adaptation to mechanical stress. Because these results were based on bioinformatic prediction, protein-level validation, including immunofluorescence staining and subcellular fractionation, is needed to confirm their localization and functions in AD.

Immune infiltration analysis showed broad neuroimmune differences between AD and control samples. DUSP4 and FREM3 were positively correlated with $CD8^+$ T cells and plasma cells,

whereas FAM107A was associated with resting natural killer (NK) cells. These correlations indicate that MSRGs may be involved in both adaptive and innate immune remodeling during AD progression. Interactions among peripheral adaptive immune cells, resident microglia, and astrocytes are increasingly recognized as part of the neuroimmune axis in AD[56]. Infiltrating $CD8^+$ T cells and antibody-producing plasma cells may contribute to chronic neuroinflammation, blood-brain barrier dysfunction, and neuronal injury[7], while activated glial cells can amplify these responses through cytokine release and immune-cell recruitment. Thus, the associations between DUSP4/FREM3 and adaptive immune populations suggest that MSRGs may influence immune-cell recruitment, activation, or retention in the AD microenvironment[16]. Since this inference was derived from transcriptomic deconvolution, spatial transcriptomics, multiplex immunofluorescence, and functional experiments will be required to determine whether these biomarkers directly regulate immune-cell trafficking and glia-immune interactions in affected brain regions.

Single-cell transcriptomic analysis indicated that astrocytes were the main cell population showing significant differential expression of all three biomarkers. This result highlights astrocytes as potential central mediators of matrix stiffness-associated remodeling. Astrocytes were the only cell type significantly linked to FREM3, DUSP4, and FAM107A, suggesting that they may act as principal mechanosensitive responders in AD. These cells are major producers of ECM components in the central nervous system and can also sense mechanical changes in the microenvironment[57, 58]. Their direct contact with the basement membrane and perivascular ECM enables rapid responses to changes in tissue stiffness. Astrocytes can undergo phenotypic transformation in response to altered ECM elasticity, cytoskeletal tension, and inflammatory

549 stress[16, 56, 59, 60]. Because of their close relationship with perivascular ECM, they are well
550 positioned to detect mechanical stress in the AD brain[59]. Concurrent dysregulation of FREM3,
551 DUSP4, and FAM107A in astrocytes may therefore link matrix stiffness abnormalities with
552 neuroinflammatory and metabolic remodeling. Astrocytes can translate mechanical cues into
553 transcriptional, inflammatory, and metabolic programs through integrin-dependent
554 mechanotransduction and cytoskeletal signaling[16, 61]. These findings suggest that astrocytes
555 may convert ECM mechanical changes into pathogenic inflammatory and metabolic responses
556 during AD progression.
557 Pseudotime analysis showed that AD astrocytes were mainly concentrated at early
558 differentiation stages, which may reflect premature pathological activation or disrupted
559 maturation. DUSP4 and FREM3 followed a dynamic "low-high-low" expression pattern,
560 whereas FAM107A increased continuously across pseudotime. These distinct trajectories
561 suggest that the biomarkers may participate in stage-specific programs during reactive astrocyte
562 activation and metabolic adaptation.
563 CellChat analysis showed stronger astrocyte-T cell communication in AD than in controls,
564 whereas these interactions were weaker under control conditions. This pattern suggests that
565 reactive astrocytes may reshape the neuroimmune microenvironment through abnormal
566 intercellular signaling. Because astrocytes produce ECM and sense mechanical cues,
567 pathological ECM stiffening may enhance inflammatory communication networks through
568 integrin-dependent mechanotransduction and cytoskeletal remodeling[62, 63], thereby promoting
569 chronic neuroinflammation and neuronal dysfunction. Astrocytes should therefore be viewed
570 as active coordinators of neuroimmune signaling rather than passive support cells. Together

with the immune infiltration results, CellChat analysis supports enhanced astrocyte-immune cell crosstalk in the AD neuroimmune microenvironment[56]. The increased astrocyte-T cell communication is consistent with evidence that adaptive immune cells and glial populations jointly contribute to chronic neuroinflammation and AD progression[7, 56]. However, these ligand-receptor interactions were inferred computationally and should be regarded as putative networks. Spatial transcriptomics, multiplex immunofluorescence, and functional validation will be needed to confirm their spatial organization and biological significance.

This study has several strengths. First, rather than focusing solely on amyloid or tau pathology, it examined AD from the perspective of matrix stiffness and ECM mechanobiology, broadening the mechanistic framework of neurodegeneration. Second, the integration of bulk transcriptomics and single-cell sequencing identified candidate biomarkers and clarified their cell-type-specific relevance, especially in astrocytes. Third, machine learning, immune infiltration analysis, and cell-cell communication analysis were combined to build a molecular framework connecting ECM remodeling, mechanotransduction, mitochondrial dysfunction, and neuroimmune activation in AD.

The identified biomarkers may also have translational relevance. Owing to their strong diagnostic performance, FREM3, DUSP4, and FAM107A may serve as candidate markers for early AD detection and disease stratification. The mechanobiological pathways identified here also suggest that targeting ECM remodeling, mechanotransduction signaling, or astrocyte-mediated inflammatory activation may offer new intervention strategies. Modulating the matrix stiffness-glial cell axis may therefore represent an alternative approach beyond conventional amyloid- or tau-centered therapies.

Several limitations should be noted. First, the analyses relied on publicly available datasets, and the biological functions of FREM3, DUSP4, and FAM107A in AD require experimental validation in vivo and in vitro. Second, although these biomarkers were associated with oxidative phosphorylation, immune regulation, and astrocyte activation, their direct regulatory relationships remain unknown. Third, the single-cell dataset contained a limited number of samples, which may affect the generalizability of the findings.

Conclusion

This study delineated matrix stiffness-related transcriptomic alterations in AD and identified FREM3, DUSP4, and FAM107A as candidate biomarkers associated with mitochondrial metabolism, immune dysregulation, and astrocyte-related cellular changes. Integrative bulk and single-cell transcriptomic analyses suggest that extracellular matrix-associated mechanical alterations may be linked to AD pathology through coordinated metabolic and neuroimmune processes, particularly those involving astrocytes. Further studies using independent clinical cohorts and experimental models are required to validate the diagnostic relevance of these genes, clarify their mechanistic roles, and determine whether the matrix stiffness–astrocyte axis represents a viable therapeutic target in AD.

Acknowledgements

The authors thank all individuals who contributed to this study.

Ethical considerations

This study exclusively used publicly available, de-identified human transcriptomic datasets obtained from the Gene Expression Omnibus database. The original studies reported

compliance with the applicable institutional ethical requirements. No additional ethical approval was required for the secondary analysis of these publicly available, de-identified data.

Consent to participate

Not applicable.

Consent for publication

Not applicable.

Author Contributions

Peida Luo: Conceptualization; Methodology; Software; Formal Analysis; Visualization; Writing—Original Draft Preparation; Writing—Review and Editing.

Yunhui Qiao: Software; Investigation; Data Curation; Writing—Review and Editing.

Chen Jin: Software; Investigation; Data Curation; Writing—Review and Editing.

Yinan Wang: Investigation; Data Curation; Writing—Review and Editing.

Yanyan Qin: Investigation; Data Curation; Writing—Review and Editing.

Yanru Wang: Investigation; Data Curation; Writing—Review and Editing.

Yunke Zhang: Conceptualization; Supervision; Project Administration; Funding Acquisition; Writing—Review and Editing.

All authors have read and approved the final version of the manuscript.

Funding

The author(s) declared that financial support was received for this work and/or its publication. This research was funded by the National Natural Science Foundation of China, grant number 81974564; the Special Scientific Research Program of Traditional Chinese Medicine for the "Double First-Class" Discipline Development of Henan Province, grant number HSRP-

DFCTCM-2023-1-04; the Central Plains Talent Program—Leading Talent Project for Scientific and Technological Innovation of Henan Province, grant number 224200510027; the Horizontal Research Project of the First Affiliated Hospital of Henan University of Chinese Medicine, grant number KY-A0739; and the 2026 Henan Provincial Special Research Program of Traditional Chinese Medicine, grant number 2026ZY3006.

Declaration of conflicting interest

The authors declared no potential conflicts of interest with respect to the research, authorship, and/or publication of this article.

Data Availability Statement

The publicly available datasets analyzed in this study can be found in the Gene Expression Omnibus under accession numbers GSE44770, GSE5281, and GSE175814. The matrix stiffness-related gene list and additional results generated during the analyses are provided in the Supplementary Material.

Supplemental material

Supplemental material for this article is available online.

References

1. Safiri S, Ghaffari Jolfayi A, Fazlollahi A, et al. Alzheimer's disease: a comprehensive review of epidemiology, risk factors, symptoms diagnosis, management, caregiving, advanced treatments and associated challenges. *Front Med (Lausanne)* 2024; 11: 1474043. 20241216. DOI: 10.3389/fmed.2024.1474043.

2. Abdul Manap AS, Almadodi R, Sultana S, et al. Alzheimer's disease: a review on the

current trends of the effective diagnosis and therapeutics. *Front Aging Neurosci* 2024; 16: 1429211. 20240809. DOI: 10.3389/fnagi.2024.1429211.

3. Wortmann M. Dementia: a global health priority - highlights from an ADI and World Health Organization report. *Alzheimers Res Ther* 2012; 4: 40. 20120921. DOI: 10.1186/alzrt143.

4. Zheng Q and Wang X. Alzheimer's disease: insights into pathology, molecular mechanisms, and therapy. *Protein Cell* 2025; 16: 83-120. DOI: 10.1093/procel/pwae026.

5. van Dyck CH, Swanson CJ, Aisen P, et al. Lecanemab in Early Alzheimer's Disease. *N Engl J Med* 2023; 388: 9-21. 20221129. DOI: 10.1056/NEJMoa2212948.

6. Sims JR, Zimmer JA, Evans CD, et al. Donanemab in Early Symptomatic Alzheimer Disease: The TRAILBLAZER-ALZ 2 Randomized Clinical Trial. *JAMA* 2023; 330: 512-527. DOI: 10.1001/jama.2023.13239.

7. Jorfi M, Maaser-Hecker A and Tanzi RE. The neuroimmune axis of Alzheimer's disease. *Genome Med* 2023; 15: 6. 20230126. DOI: 10.1186/s13073-023-01155-w.

8. Anwar MM, Özkan E and Gürsoy-Özdemir Y. The role of extracellular matrix alterations in mediating astrocyte damage and pericyte dysfunction in Alzheimer's disease: A comprehensive review. *Eur J Neurosci* 2022; 56: 5453-5475. 20210705. DOI: 10.1111/ejn.15372.

9. Discher DE, Janmey P and Wang YL. Tissue cells feel and respond to the stiffness of their substrate. *Science* 2005; 310: 1139-1143. DOI: 10.1126/science.1116995.

10. Freedman BR, Bade ND, Riggin CN, et al. The (dys)functional extracellular matrix. *Biochim Biophys Acta* 2015; 1853: 3153-3164. 20150427. DOI: 10.1016/j.bbamcr.2015.04.015.

11. Courbot O and Elosegui-Artola A. The role of extracellular matrix viscoelasticity in

development and disease. *NPJ Biol Phys Mech* 2025; 2: 10. 20250403. DOI: 10.1038/s44341-025-00014-6.

12. Deng B, Zhao Z, Kong W, et al. Biological role of matrix stiffness in tumor growth and treatment. *J Transl Med* 2022; 20: 540. 20221122. DOI: 10.1186/s12967-022-03768-y.

13. Guo T, Wantono C, Tan Y, et al. Regulators, functions, and mechanotransduction pathways of matrix stiffness in hepatic disease. *Front Physiol* 2023; 14: 1098129. 20230112. DOI: 10.3389/fphys.2023.1098129.

14. Samara A and Ontaneda D. Evolving the Diagnosis of Multiple Sclerosis: A New Landscape in Light of the 2024 McDonald Criteria. *Biomedicines* 2025; 13 20251023. DOI: 10.3390/biomedicines13112590.

15. Saraswathibhatla A, Indana D and Chaudhuri O. Cell-extracellular matrix mechanotransduction in 3D. *Nat Rev Mol Cell Biol* 2023; 24: 495-516. 20230227. DOI: 10.1038/s41580-023-00583-1.

16. Huber RE, Babbitt C and Peyton SR. Heterogeneity of brain extracellular matrix and astrocyte activation. *J Neurosci Res* 2024; 102: e25356. DOI: 10.1002/jnr.25356.

17. Liu Y, Zhang J, Li Y, et al. Matrix stiffness-dependent microglia activation in response to inflammatory cues: in situ investigation by scanning electrochemical microscopy. *Chem Sci* 2023; 15: 171-184. 20231128. DOI: 10.1039/d3sc03504b.

18. Kwok JCF and Dityatev A. Extracellular matrix remodelling in neurological diseases. *Nat Rev Neurol* 2026 20260422. DOI: 10.1038/s41582-026-01209-8.

19. Li H, Zhang J, Shi Y, et al. Identification of matrix stiffness-related molecular subtypes in HCC via integrating multi-omics analysis and machine learning algorithms. *J Transl Med* 2025;

701 23: 716. 20250701. DOI: 10.1186/s12967-025-06733-7.

702 20. Ritchie ME, Phipson B, Wu D, et al. limma powers differential expression analyses for
703 RNA-sequencing and microarray studies. *Nucleic Acids Res* 2015; 43: e47. 20150120. DOI:
704 10.1093/nar/gkv007.

705 21. Gustavsson EK, Zhang D, Reynolds RH, et al. ggtranscript: an R package for the
706 visualization and interpretation of transcript isoforms using ggplot2. *Bioinformatics* 2022; 38:
707 3844-3846. DOI: 10.1093/bioinformatics/btac409.

708 22. Gu Z and Hubschmann D. Make Interactive Complex Heatmaps in R. *Bioinformatics* 2022;
709 38: 1460-1462. DOI: 10.1093/bioinformatics/btab806.

710 23. Zheng Y, Gao W, Zhang Q, et al. Ferroptosis and Autophagy-Related Genes in the
711 Pathogenesis of Ischemic Cardiomyopathy. *Front Cardiovasc Med* 2022; 9: 906753. 20220630.
712 DOI: 10.3389/fcvm.2022.906753.

713 24. Yu G, Wang LG, Han Y, et al. clusterProfiler: an R package for comparing biological
714 themes among gene clusters. *OMICS* 2012; 16: 284-287. 20120328. DOI:
715 10.1089/omi.2011.0118.

716 25. Friedman J, Hastie T and Tibshirani R. Regularization Paths for Generalized Linear Models
717 via Coordinate Descent. *J Stat Softw* 2010; 33: 1-22.

718 26. Alderden J, Pepper GA, Wilson A, et al. Predicting Pressure Injury in Critical Care Patients:
719 A Machine-Learning Model. *Am J Crit Care* 2018; 27: 461-468. DOI: 10.4037/ajcc2018525.

720 27. Zhang Z, Zhao Y, Canes A, et al. Predictive analytics with gradient boosting in clinical
721 medicine. *Ann Transl Med* 2019; 7: 152. DOI: 10.21037/atm.2019.03.29.

722 28. Jia A, Xu L and Wang Y. Venn diagrams in bioinformatics. *Brief Bioinform* 2021; 22. DOI:

723 10.1093/bib/bbab108.

724 29. Sachs MC. plotROC: A Tool for Plotting ROC Curves. *J Stat Softw* 2017; 79 20170809.
725 DOI: 10.18637/jss.v079.c02.

726 30. Robin X, Turck N, Hainard A, et al. pROC: an open-source package for R and S+ to analyze
727 and compare ROC curves. *BMC Bioinformatics* 2011; 12: 77. 20110317. DOI: 10.1186/1471-
728 2105-12-77.

729 31. N'Dilimabaka N, Mounguegui DM, Lekana-Douki SE, et al. Biochemical and
730 hematological factors associated with COVID-19 severity among Gabonese patients: A
731 retrospective cohort study. *Front Cell Infect Microbiol* 2022; 12: 975712. 20221223. DOI:
732 10.3389/fcimb.2022.975712.

733 32. Newman AM, Liu CL, Green MR, et al. Robust enumeration of cell subsets from tissue
734 expression profiles. *Nat Methods* 2015; 12: 453-457. 20150330. DOI: 10.1038/nmeth.3337.

735 33. Satija R, Farrell JA, Gennert D, et al. Spatial reconstruction of single-cell gene expression
736 data. *Nat Biotechnol* 2015; 33: 495-502. 20150413. DOI: 10.1038/nbt.3192.

737 34. Zhang L, Cui X and Huang H. Identification of common pathway and hub genes in the
738 degeneration of both annulus fibrosus and nucleus pulposus in intervertebral disc. *J Orthop*
739 *Surg (Hong Kong)* 2023; 31: 10225536231167705. DOI: 10.1177/10225536231167705.

740 35. Hanzelmann S, Castelo R and Guinney J. GSVA: gene set variation analysis for microarray
741 and RNA-seq data. *BMC Bioinformatics* 2013; 14: 7. 20130116. DOI: 10.1186/1471-2105-14-
742 7.

743 36. Qiu X, Hill A, Packer J, et al. Single-cell mRNA quantification and differential analysis
744 with Census. *Nat Methods* 2017; 14: 309-315. 20170123. DOI: 10.1038/nmeth.4150.

745 37. Jin S, Plikus MV and Nie Q. CellChat for systematic analysis of cell-cell communication
746 from single-cell transcriptomics. *Nat Protoc* 2025; 20: 180-219. 20240916. DOI:
747 10.1038/s41596-024-01045-4.
748 38. Alves F, Lane D, Wahida A, et al. Aberrant Mitochondrial Metabolism in Alzheimer's
749 Disease Links Energy Stress with Ferroptosis. *Adv Sci (Weinh)* 2025; 12: e04175. 20250708.
750 DOI: 10.1002/advs.202504175.
751 39. Kechagia JZ, Ivaska J and Roca-Cusachs P. Integrins as biomechanical sensors of the
752 microenvironment. *Nat Rev Mol Cell Biol* 2019; 20: 457-473. DOI: 10.1038/s41580-019-0134-
753 2.
754 40. Geiger B, Spatz JP and Bershadsky AD. Environmental sensing through focal adhesions.
755 *Nat Rev Mol Cell Biol* 2009; 10: 21-33. DOI: 10.1038/nrm2593.
756 41. Jahed Z, Shams H, Mehrbod M, et al. Mechanotransduction pathways linking the
757 extracellular matrix to the nucleus. *Int Rev Cell Mol Biol* 2014; 310: 171-220. DOI:
758 10.1016/B978-0-12-800180-6.00005-0.
759 42. Nikolova YS, Iruku SP, Lin CW, et al. FRAS1-related extracellular matrix 3 (FREM3)
760 single-nucleotide polymorphism effects on gene expression, amygdala reactivity and perceptual
761 processing speed: An accelerated aging pathway of depression risk. *Front Psychol* 2015; 6:
762 1377. 20150916. DOI: 10.3389/fpsyg.2015.01377.
763 43. Arevalo A, Baldo J, Gonzalez-Perilli F, et al. Editorial: What can we make of theories of
764 embodiment and the role of the human mirror neuron system? *Front Hum Neurosci* 2015; 9:
765 500. 20150911. DOI: 10.3389/fnhum.2015.00500.
766 44. Li Z and Chen B. DUSP4 alleviates LPS-induced chondrocyte injury in knee osteoarthritis

via the MAPK signaling pathway. *Exp Ther Med* 2021; 22: 1401. 20211001. DOI: 10.3892/etm.2021.10837.

45. Huang H, Liao H, Chen Y, et al. Disruption of the Clock Component BMAL1 in HDM-induced Asthma Causes GC Resistance in Airway Epithelial Cells by Regulating GR Phosphorylation through the DUSP4-p38MAPK Pathway. *Int J Biol Sci* 2025; 21: 6482-6500. 20251010. DOI: 10.7150/ijbs.119486.

46. Dougherty JA, Kilbane Myers J, Khan M, et al. Dual-Specificity Phosphatase 4 Overexpression in Cells Prevents Hypoxia/Reoxygenation-Induced Apoptosis via the Upregulation of eNOS. *Front Cardiovasc Med* 2017; 4: 22. 20170424. DOI: 10.3389/fcvm.2017.00022.

47. Almerdhemah H, Mulla Z, Muamenah HM, et al. Site-Specific Education Using Digital Media to Improve Patient Understanding of the Radiotherapy Trajectory: An Interventional Study. *Adv Radiat Oncol* 2021; 6: 100742. 20211026. DOI: 10.1016/j.adro.2021.100742.

48. Wang Z, Gao X, Ji H, et al. Characterization of gut microbiota and metabolites in renal transplant recipients during COVID-19 and prediction of one-year allograft function. *J Transl Med* 2025; 23: 420. 20250410. DOI: 10.1186/s12967-025-06090-5.

49. Nakajima H and Koizumi K. Family with sequence similarity 107: A family of stress responsive small proteins with diverse functions in cancer and the nervous system (Review). *Biomed Rep* 2014; 2: 321-325. 20140227. DOI: 10.3892/br.2014.243.

50. Xu C, Dong Y, Li J, et al. Integrating machine learning and Mendelian randomization for identifying genetic biomarkers in bladder cancer: implications for early diagnosis and targeted therapies. *Int J Surg* 2026; 112: 2969-2987. 20251203. DOI: 10.1097/JS9.0000000000003833.

789 51. Zhang J, Di S, Li M, et al. FAM107A as a tumor suppressor in esophageal squamous
790 carcinoma inhibits growth and metastasis. *Pathol Res Pract* 2023; 252: 154945. 20231111. DOI:
791 10.1016/j.prp.2023.154945.
792 52. Johnson ECB, Carter EK, Dammer EB, et al. Large-scale deep multi-layer analysis of
793 Alzheimer's disease brain reveals strong proteomic disease-related changes not observed at the
794 RNA level. *Nat Neurosci* 2022; 25: 213-225. 20220203. DOI: 10.1038/s41593-021-00999-y.
795 53. Timon-Gomez A, Doerrier C, Sumbalova Z, et al. Bioenergetic profiles and respiratory
796 control in mitochondrial physiology: Precision analysis of oxidative phosphorylation. *Exp*
797 *Physiol* 2026; 111: 179-211. 20250801. DOI: 10.1113/EP092792.
798 54. Bell SM, Barnes K, De Marco M, et al. Mitochondrial Dysfunction in Alzheimer's Disease:
799 A Biomarker of the Future? *Biomedicines* 2021; 9 20210111. DOI:
800 10.3390/biomedicines9010063.
801 55. Hung CT, Racine-Avila J, Pellicore MJ, et al. Biophysical Modulation of Mesenchymal
802 Stem Cell Differentiation in the Context of Skeletal Repair. *Int J Mol Sci* 2022; 23 20220401.
803 DOI: 10.3390/ijms23073919.
804 56. Linnerbauer M, Wheeler MA and Quintana FJ. Astrocyte Crosstalk in CNS Inflammation.
805 *Neuron* 2020; 108: 608-622. 20200907. DOI: 10.1016/j.neuron.2020.08.012.
806 57. Gonzalez-Perez O, Lopez-Virgen V and Quinones-Hinojosa A. Astrocytes: Everything but
807 the glue. *Neuroimmunol Neuroinflamm* 2015; 2: 115-117. DOI: 10.4103/2347-8659.153979.
808 58. Jimenez-Vergara AC, Avina J, Block TJ, et al. A Bioinspired Astrocyte-Derived Coating
809 Promotes the In Vitro Proliferation of Human Neural Stem Cells While Maintaining Their
810 Stemness. *Biomimetics (Basel)* 2023; 8 20231204. DOI: 10.3390/biomimetics8080589.

811 59. Turovsky EA, Braga A, Yu Y, et al. Mechanosensory Signaling in Astrocytes. *J Neurosci*
812 2020; 40: 9364-9371. 20201029. DOI: 10.1523/JNEUROSCI.1249-20.2020.
813 60. Pogoda K and Janmey PA. Glial Tissue Mechanics and Mechanosensing by Glial Cells.
814 *Front Cell Neurosci* 2018; 12: 25. 20180221. DOI: 10.3389/fncel.2018.00025.
815 61. Anwar MM, Ozkan E and Gursoy-Ozdemir Y. The role of extracellular matrix alterations
816 in mediating astrocyte damage and pericyte dysfunction in Alzheimer's disease: A
817 comprehensive review. *Eur J Neurosci* 2022; 56: 5453-5475. 20210705. DOI:
818 10.1111/ejn.15372.
819 62. Schwartz MA. Integrins and extracellular matrix in mechanotransduction. *Cold Spring*
820 *Harb Perspect Biol* 2010; 2: a005066. 20101117. DOI: 10.1101/cshperspect.a005066.
821 63. Geiger B, Bershadsky A, Pankov R, et al. Transmembrane crosstalk between the
822 extracellular matrix--cytoskeleton crosstalk. *Nat Rev Mol Cell Biol* 2001; 2: 793-805. DOI:
823 10.1038/35099066.

824

825 **List of abbreviations**

Abbreviation	Full term
AD	Alzheimer’s disease
Aβ	β-amyloid
AUC	Area under the curve
BP	Biological process
CC	Cellular component

DEGs	Differentially expressed genes
ECM	Extracellular matrix
FC	Fold change
GEO	Gene Expression Omnibus
GO	Gene Ontology
GSEA	Gene set enrichment analysis
KEGG	Kyoto Encyclopedia of Genes and Genomes
LASSO	Least absolute shrinkage and selection operator
MS	Matrix stiffness
MSRGs	Matrix stiffness-related genes
NFTs	Neurofibrillary tangles
PCA	Principal component analysis
PPI	Protein-protein interaction
RF	Random forest
ROC	Receiver operating characteristic
scRNA-seq	Single-cell RNA sequencing
SVM-RFE	Support vector machine-recursive feature elimination
TF	Transcription factor
UMAP	Uniform manifold approximation and projection

826

Supplementary Files

This is a list of supplementary files associated with this preprint. Click to download.

- SupplementaryFiles.zip